ACS APPLIED MATERIALS & INTERFACES

Research Article

www.acsami.org

Effects of Metal Composition and Ratio on Peptide-Templated Multimetallic PdPt Nanomaterials

Nicholas A. Merrill,[†] Tadeusz T. Nitka,[‡] Erik M. McKee,[†] Kyle C. Merino,[†] Lawrence F. Drummy,[§] Sungsik Lee,[∥] Benjamin Reinhart,[∥] Yang Ren,[∥] Catherine J. Munro,[†] Svitlana Pylypenko,[‡] Anatoly I. Frenkel,[*,⊥] Nicholas M. Bedford,[*,†,§,#] and Marc R. Knecht[*,†]

[†]Department of Chemistry, University of Miami, 1301 Memorial Drive, Coral Gables, Florida 33146, United States

[‡]Department of Chemistry, Colorado School of Mines, Golden, Colorado 80401, United States

[§]Materials and Manufacturing Directorate, Air Force Research Laboratory, Wright-Patterson Air Force Base, Ohio 45433, United States

[∥]X-ray Science Division, Argonne National Laboratory, 9700 South Cass Avenue, Argonne, Illinois 60439, United States

[⊥]Department of Materials Science and Chemical Engineering, Stony Brook University, Stony Brook, New York 11794, United States

[#]Applied Chemicals and Materials Division, National Institute of Standards and Technology, Boulder, Colorado 80305, United States

Supporting Information

ABSTRACT: It can be difficult to simultaneously control the size, composition, and morphology of metal nanomaterials under benign aqueous conditions. For this, bioinspired approaches have become increasingly popular due to their ability to stabilize a wide array of metal catalysts under ambient conditions. In this regard, we used the R5 peptide as a three-dimensional template for formation of PdPt bimetallic nanomaterials. Monometallic Pd and Pt nanomaterials have been shown to be highly reactive toward a variety of catalytic processes, but by forming bimetallic species, increased catalytic activity may be realized. The optimal metal-to-metal ratio was determined by varying the Pd:Pt ratio to obtain the largest increase in catalytic activity. To better understand the morphology and the local atomic structure of the materials, the bimetallic PdPt nanomaterials were extensively studied by transmission electron microscopy, extended X-ray absorption fine structure spectroscopy, X-ray photoelectron spectroscopy, and pair distribution function analysis. The resulting PdPt materials were determined to form multicomponent nanostructures where the Pt component demonstrated varying degrees of oxidation based upon the Pd:Pt ratio. To test the catalytic reactivity of the materials, olefin hydrogenation was conducted, which indicated a slight catalytic enhancement for the multicomponent materials. These results suggest a strong correlation between the metal ratio and the stabilizing biotemplate in controlling the final materials morphology, composition, and the interactions between the two metal species.

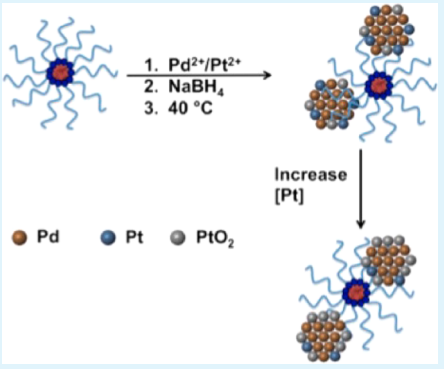

KEYWORDS: *peptides, nanoparticle, bimetallic, catalysis, X-ray characterization, atomic characterization*

INTRODUCTION

Catalytic technologies remain of great importance; however, without extensive enhancements, many reaction systems will no longer be employable due to their energy consumption. As such, reaction efficiencies must be significantly improved, where the design of multicomponent catalytic materials is imperative. Single and multicomponent nanoparticle catalysts have been extensively studied for numerous reactions[1−4] due to their unique properties at the nanoscale arising from their enhanced surface-to-volume ratio.[5] Among these, Pd, Pt, and PtO_2 are known to be versatile catalysts for a wide variety of reactions, including olefin hydrogenation,[2,6,7] C−C couplings,[1,8,9] and oxygen reduction reactions.[3] While these catalysts are extensively exploited, many limitations hinder their widespread use, such as catalyst cost and lifetime.

To enhance catalytic reactivity, multicomponent materials have been explored, including bimetallic nanoparticles and metal/metal oxide composites.[10−14] Bimetallic nanomaterials have demonstrated enhanced reactivity due to two factors: (1) electronic effects of the composite materials and (2) the geometric arrangement of the two metal atoms.[15] Conversely, metal/metal oxide combinations have also been shown to enhance catalytic properties due to synergistic properties accessed at the interface between the two components.[13,16−19] At this interface, the properties of both materials are altered, most likely due to electron transfer effects,[17,18]

Received: September 13, 2016
Accepted: February 3, 2017
Published: February 3, 2017

DOI: 10.1021/acsami.6b11651
ACS Appl. Mater. Interfaces 2017, 9, 8030−8040

surface rearrangement,[12,19] and lattice mismatch-induced crystal strain.[20,21] While synthetic approaches have been explored for the generation of both bimetallic and metal/metal oxide structures,[12,13,15,22] they typically rely upon energy-intensive methods that require multiple synthetic steps. It would be ideal to identify a universal approach that could be applied to different materials of multiple compositions to generate final structures with predictable compositions, morphologies, and arrangements. Unfortunately, such approaches remain elusive.

Converse to traditional syntheses, bioinspired approaches offer advantageous routes to harness the structural diversity and customizability offered by biomolecules for the generation of multicomponent inorganic nanomaterials.[23,24] From this, tunable surface features could be realized that serve as active sites for catalytic reactions.[25,26] Common bioinspired approaches include the use of peptides,[9,27] viruses,[28−31] and proteins[32−35] as templates, whose structures can be manipulated. For example, Heilshorn and co-workers[36−38] have used peptides to modify clathrin protein cages to template metal nanoparticles. In other work, Belcher and co-workers[30,39−41] have extensively studied the M13 bacteriophage as a template for the fabrication of metallic and metal oxide materials of various compositions. For this, the researchers used the virus as a template to synthesize nanowires by genetically engineering the coat protein to express short peptide sequences to bind metal species along the long phage axis, resulting in nanowire production.[28,40]

While protein cages and viruses can template nanomaterials, multifunctional peptides may represent a versatile and simpler platform. In this regard, the R5 peptide (SSKKSGSYSGSKGSKRRIL), isolated from the diatom *Cylindrothica fusiformis*,[42,43] is unique as it self-assembles in water to form a scaffold due to the hydrophobic RRIL motif.[1,2,9] The hydrophobic residues are constrained at the core of the framework, displaying the hydrophilic residues to bind with metal ions. Upon reduction, the formation of monometallic (Pd,[1,2,9,44] Pt,[2] and Au[45]) and bimetallic (PdAu[10]) nanomaterials has been achieved. The morphology of the final structures is controlled by the amount of metal ions in the reaction, as well as their composition and ratio for the bimetallic PdAu system.[1,2,9] For instance, for Pd monometallic structures, at low Pd loadings, spherical particles are generated that grow into nanoparticle networks (NPNs) at higher loadings.[2,9] Previous studies of the R5-templated monometallic Pd and Pt materials for the hydrogenation of allyl alcohol demonstrated high turnover frequency (TOF) values of ∼2900 and ∼800 mol product (mol metal × h)$^{-1}$ for these structures, respectively.[2] When bimetallic PdAu nanomaterials were generated with this biotemplate, significantly enhanced reactivity was noted.[10] In this regard, when the bimetallic structures were composed of 33% Au, a 2-fold increase in the TOF value was noted, arising from electronic changes to the alloyed structure.[10] Similar materials have been prepared by use of polymeric templates[46,47] or even mesoporous inorganic templates[48] that are comparable to the R5 template of the present work. To this end, Yamauchi and co-workers[46,47] have used polymeric templates to generate Pd monometallic and PdPt bimetallic structures where the polymer served as the structure-controlling template.

Here we report on the formation, structural elucidation, and catalytic properties of R5-templated PdPt-based materials in which the Pt component displays surprising degrees of oxidation that depends upon the Pd:Pt ratio employed. For these materials, spherical multicomponent nanoparticles were generated that were embedded within the peptide framework. The materials were extensively characterized by atomic-scale techniques such as transmission electron microscopy (TEM) with energy-dispersive X-ray spectroscopy (EDS) mapping, X-ray absorption fine-structure spectroscopy (XAFS), atomic pair distribution function (PDF) analysis of high-energy X-ray diffraction (HE-XRD) patterns, and X-ray photoelectron spectroscopy (XPS). For all materials, the Pd:Pt ratio was varied to explore the effects of metal loading on the final material structure and composition. Surprisingly, while the Pd component is observed to be fully reduced, the Pt component tends to be partially oxidized at high Pt loadings. The oxidized Pt species are likely located at the particle surface containing a bimetallic PdPt core. These reduction effects are likely influenced by the binding of the peptide to the metal ions before reduction. By examining the atomic makeup of the materials via a combination of high-resolution characterization techniques, key evidence regarding the atomic composition and structure of the materials can be elucidated to better understand the formation of multicomponent inorganic materials and to correlate these structural effects to the observed catalytic reactivity.

MATERIALS AND METHODS

Chemicals. Allyl alcohol (>99%), 3-buten-2-ol (97%), 2-methyl-3-buten-2-ol (98%), K_2PdCl_4 (98%), K_2PtCl_4 (46−47% Pt), and antifoam SE-15 were purchased from Sigma−Aldrich, while $NaBH_4$ (98%) was acquired from Acros Organics. Peptide synthesis materials, including Wang resins and fluorenylmethyloxycarbonyl (Fmoc)-protected amino acids, were purchased from Advanced Chemtech. Acetonitrile, methanol, and *N*,*N*-dimethylformamide (DMF) were purchased from VWR, all of which were ACS-grade. All materials were used as received, and Milli-Q water (18 MΩ·cm) was used for all aqueous experiments.

Peptide Synthesis. Standard Fmoc protocols were used to synthesize the R5 peptide, which was purified by reverse-phase high-performance liquid chromatography (HPLC).[49] Matrix-assisted laser desorption ionization time-of-flight (MALDI-TOF) mass spectrometry was employed to confirm the peptide sequence.

Fabrication of Peptide-Templated Metal/Metal Oxide Materials. Nanoparticle synthesis was adapted from previously published methods.[2,9,10] The multicomponent materials were synthesized at a 60:1 total metal:peptide ratio, where the Pd:Pt ratio was 1:0, 5:1, 2:1, 1:1, 1:2, 1:3, or 0:1. In brief, to 3.00 mL of water was added 4.93 μL of a 10 mg/mL R5 stock solution. Next, 14.70, 12.25, 9.80, 7.35, 4.90, 3.68, or 0.00 μL of a 0.10 M aqueous stock solution of K_2PdCl_4 was added to the reaction mixture. This was followed by 0.00, 2.45, 4.90, 7.35, 9.80, 11.03, or 14.70 μL of a 0.10 M aqueous stock of K_2PtCl_4 for each reaction, respectively. The solution was briefly agitated at room temperature, allowed to complex for 15 min, followed by the addition of 75.0 μL of a freshly prepared aqueous 0.10 M $NaBH_4$ solution. The materials were reduced for 24.0 h under constant vigorous stirring at 40 °C.

Catalytic Hydrogenation. Catalytic hydrogenation of olefinic alcohols was conducted with minor variations from previously published procedures.[2,6,50] In short, to 23.72 mL of H_2O in a 250 mL three-necked round-bottom flask was added 1.28 mL of the peptide-templated multicomponent material, along with 20.0 μL of antifoam SE-15. The solution was then bubbled with H_2 gas through a gas dispersion tube at 50 kPa gauge pressure for 30 min to saturate the inorganic surface with hydrogen. To initiate the reaction, 25.0 mL of a 50.0 mM olefinic alcohol solution was added to the reaction, resulting in a catalyst loading of 0.05 mol % metal. A 0.0 min time point aliquot was immediately extracted, followed by successive aliquot removals at 1, 5, 10, 15, 20, 30, 40, 50, and 60 min. TOF values were obtained by analyzing the aliquots via gas chromatography (Agilent 7820A)

DOI: 10.1021/acsami.6b11651
ACS Appl. Mater. Interfaces 2017, 9, 8030−8040

equipped with a DB-ALC1 column and a flame ionization detector.[2,6,50]

Characterization. All UV−vis spectra were obtained on an Agilent 8453 spectrometer employing a 2.0 mm quartz cuvette. The cuvettes were cleaned with aqua regia before use. A Phillips CM200 TEM operating at 200 kV was used for lower-resolution TEM analysis. Energy-dispersive X-ray spectroscopy (EDS) mapping experiments were performed on a FEI Talos F200S. HE-XRD experiments were performed at the 11-ID-C beamline of the Advanced Photon Source, Argonne National Laboratory. For this analysis, lyophilized powders were placed in 2 mm quartz capillaries to obtain diffraction patterns at very high Q (~45 $Å^{-1}$) with 115 keV irradiation. HE-XRD patterns were corrected for background scattering, converted into $F(Q)$, and Fourier-transformed into PDFs by use of the program RAD.[51] XAFS was performed at the 12-BM beamline, Advanced Photon Source, Argonne National Laboratory. Lyophilized powders were spread across scotch tape for analysis, and both the Pd K-edge and Pt L_3 edge were examined from 200 eV before to 900 eV after each element adsorption edge by use of a 13-channel Ge detector. Modeling of the Pd and Pt extended XAFS data was performed by use of the Artemis program employing FEFF6 theory.[52] Standard foils were analyzed to obtain S_0^2 values of 0.817 and 0.824 for Pd and Pt, respectively, which were used for extended XAFS modeling of nanomaterial samples. XPS was performed on a Kratos Axis Nova spectrometer with a hemispherical energy analyzer and monochromatic Al Kα source. The high-resolution spectra of C 1s, O 1s, Pt 4f, and Pd 3d were acquired with pass energy of 20 eV. Both Pt 4f and Pd 3d spectra were smoothed prior to Shirley background subtraction. Spectra were decomposed with 70%/30% Gaussian/Lorentzian peaks constrained to 1.5 eV for Pt 4f and 1.3 eV for Pd 3d. Data analysis and quantification were performed by use of CasaXPS software.

RESULTS AND DISCUSSION

The R5 peptide assembles to form a large bioscaffold in water where the polar residues can complex metal ions and support the formation of inorganic nanomaterials.[1,2,9,50] To facilitate the production of bimetallic nanomaterials, Pd^{2+} and Pt^{2+} ions were mixed with the template in solution, followed by reduction with $NaBH_4$ at 40 °C for 24 h. Individual Pd and Pt nanoparticles were similarly synthesized.[2] Sequential reduction methods[11,53] (i.e., reduce one metal followed by the second) could not be examined due to destabilization of the complex during the secondary reduction step. All materials were synthesized at a 60:1 metal ion:peptide ratio, where the Pd:Pt ratio varied from 100:0 to 0:100. To distinguish the samples by metal ratio, the materials will be referred to as Pd_xPt_y, where x and y represent the Pd and Pt mole fractions in the sample out of 100. The monometallic species are termed Pd_{100} or Pt_{100}.

To characterize the metal−peptide interactions before and after nanoparticle synthesis, UV−vis spectra of the materials were obtained (Figure 1). Figure 1a specifically shows the UV−vis spectra before reduction for the bimetallic nanomaterials. A ligand-to-metal charge transfer (LMCT) band was observed at 235 nm for the monometallic Pd structures, corresponding to the interaction between Pd^{2+} ions and the peptide template.[9] As Pt^{2+} was introduced into the system, with a concurrent decrease in the Pd^{2+} loading, a change in the UV−vis spectrum was observed. To this end, diminishment of the Pd^{2+} LMCT band was observed with formation of a new peak at 216 nm, corresponding to Pt^{2+} ions within the peptide template. Upon reduction (Figure 1b), the absorbances arising from peptide-coordinated Pd^{2+} and Pt^{2+} ions were no longer observed, while the formation of a featureless spectrum for each material was noted. For each nanomaterial sample, a spectrum with an increase toward lower wavelengths was observed, consistent with the formation of nanomaterials.[54]

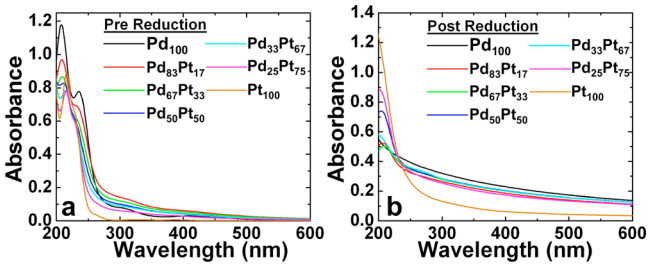

Figure 1. UV−vis analysis of the R5-templated PdPt structures (a) before and (b) after reduction with $NaBH_4$.

TEM was next used to analyze the morphology and size of the peptide-templated materials (Figure 2). Interestingly, for all structures, nearly spherical nanoparticles were noted; however, the structures were generally polydisperse in morphology. Unfortunately, due to residual carbon degrading during TEM imaging, higher-resolution TEM images could not be achieved. The morphology effects were somewhat surprising, as changes in metal loading or composition typically result in changes in material morphology;[9,25] however, Pt-based structures fabricated from the R5 template are known to be spherical regardless of the metal concentration in the reaction.[2] When the Pd_{100} materials were considered, as shown in Figure 2a, spherical nanoparticles of 3.0 ± 0.7 nm were observed, consistent with previous studies.[1,2,10,44] As Pt was incorporated into the materials, the size of the particles slightly increased to 3.2 ± 0.8 and 4.3 ± 0.6 nm for $Pd_{83}Pt_{17}$ and $Pd_{67}Pt_{33}$ samples, respectively (Figure 2b,c). Upon further increasing the Pt loading, the size of the materials began to decrease to 3.8 ± 0.6, 3.7 ± 0.7, 3.6 ± 0.7, and 1.7 ± 0.3 nm for the $Pd_{50}Pt_{50}$, $Pd_{33}Pt_{67}$, $Pd_{25}Pt_{75}$, and Pt_{100} materials, respectively (Figure 2d−g). For ease in comparison, Figure 2h presents a plot of the change in particle size as a function of Pd composition.

While the overall size and general morphology of the different materials can be assessed by TEM, to determine the atomic-level interactions, structure, composition, and metallic oxidation state, other methods are required. As a primary study, EDS mapping was conducted on all PdPt materials to visually observe the level of metal atom mixing within the material, as shown in Figure 3. The top row of Figure 3 specifically presents the analysis for $Pd_{83}Pt_{17}$ nanoparticles; the panel on the left is the scanning transmission electron microscopic (STEM) image, while the middle and right panels present the elemental maps for Pd and Pt, respectively. When the Pd and Pt maps are compared, an even overall distribution of each metal is noted, suggestive of materials of mixed Pd and Pt composition. Such a structure was anticipated due to the coreduction of Pt^{2+} and Pd^{2+} metal ions, which has been shown to form alloyed nanoparticles.[55] Additional STEM imaging and EDS mapping analysis are presented in Figure 3 for all PdPt structures, which were all consistent with the $Pd_{83}Pt_{17}$ materials. While EDS mapping suggests an alloyed particle, the data are insensitive to oxidation state, limited in resolution (especially for nanoparticles of this size), and can be completed only on a global particle level; additional high-resolution studies are required to fully elucidate the atomic-level interactions between Pd and Pt, as well as their oxidation state, within the nanostructure.

To further probe the atomic structure of the multicomponent materials, XAFS, XPS, and HE-XRD coupled to PDF analysis were performed. XAFS can reveal element-specific

DOI: 10.1021/acsami.6b11651
ACS Appl. Mater. Interfaces 2017, 9, 8030−8040

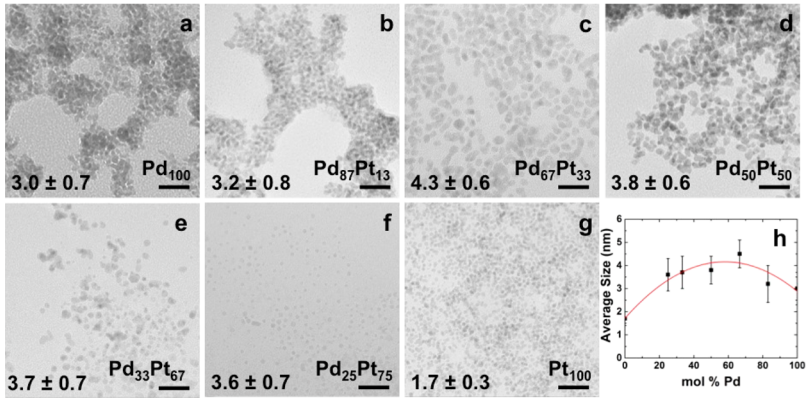

Figure 2. TEM images of (a) Pd_{100}, (b) $Pd_{87}Pt_{17}$, (c) $Pd_{67}Pt_{33}$, (d) $Pd_{50}Pt_{50}$, (e) $Pd_{33}Pt_{67}$, (f) $Pd_{25}Pt_{75}$, and (g) Pt_{100} samples. (h) Change in particle size as a function of Pd composition. Scale bar = 20 nm.

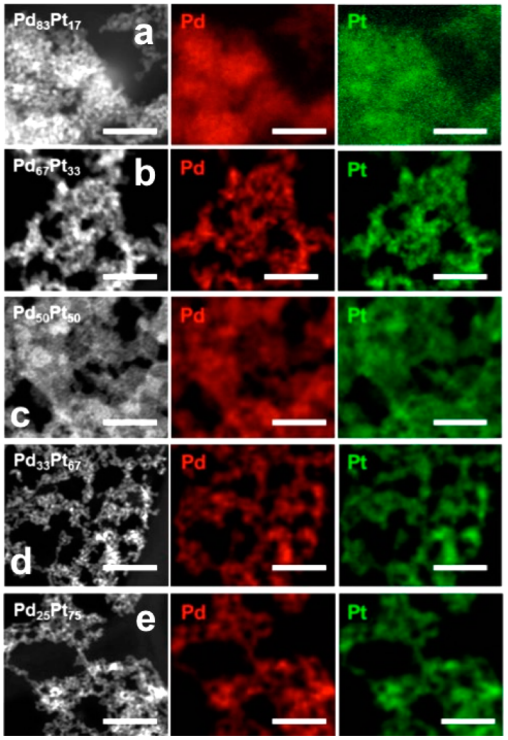

Figure 3. EDS mapping analysis of (a) $Pd_{83}Pt_{17}$, (b) $Pd_{67}Pt_{33}$, (c) $Pd_{50}Pt_{50}$, (d) $Pd_{33}Pt_{67}$, and (e) $Pd_{25}Pt_{75}$ materials. The left panel presents the STEM image of the structure that was mapped, while the middle and right panels display Pd and Pt maps, respectively. Scale bar = 50 nm.

structural and chemical information, which is particularly difficult to ascertain for multicomponent nanomaterials. The X-ray absorption near-edge structure (XANES) at the Pd K edge for all nanomaterials and a reference Pd foil (Figure 4a) indicate that the Pd atoms are largely zerovalent; minimal deviations in the spectra for Pd_{100} and all multicomponent materials are noted. In fully miscible bimetallic NPs (i.e., alloyed structures), small shifts in the XANES spectrum can be observed as the ratio between metals is varied.[22,56,57] Interestingly, in the present study, such shifts were not noted. Conversely, the XANES spectra at the Pt L_3 edge (Figure 4b) demonstrate incomplete Pt reduction, particularly in Pt_{100}. Indeed, Pt_{100} exhibits higher white line intensities than any of the alloyed nanoparticles and the reference Pt foil and is more similar in post-edge features to reference PtO_2 than to Pt foil. For the alloyed materials, the white line intensities are higher than those for the Pt foil. This indicates that the Pt in the multicomponent materials is partially oxidized, while Pt_{100} is heavily oxidized. Subsequent extended X-ray absorption fine structure (EXAFS) modeling further corroborates the observed trends in Pt-XANES.

EXAFS spectra from the Pd K edge and Pt L_3 edge (Figure 4c,d) further suggest the presence of Pd-concentration-dependent Pt oxidation. Fourier transform magnitudes of Pd K edge EXAFS spectra have a main peak at 2.45 Å, which is shifted to lower distances compared to real-space distance between nearest-neighbor Pd atoms (e.g., 2.74 Å in the bulk) due to the photoelectron phase shift. As the amount of Pt is increased in R5-templated nanomaterials, a slight shift of the first nearest-neighbor peak to longer distances is noted, consistent with the presence of the longer (Pd−Pt) contribution to the first shell peak, given that the first coordination sphere distance in bulk Pt is 2.77 Å. Note that there is no obvious Pd − low-Z feature, which indicates that the Pd is zerovalent and that it is not strongly interacting with low-Z atoms, such as the templating R5 peptide or unreduced $PdCl_4^{2-}$.[58] Conversely, the Pt EXAFS (Figure 4d) confirms an amount of metallic, zerovalent Pt atoms within the sample that is lower than the anticipated loading amount. For instance, Pt_{100} has no observable metallic bonding but instead has a very strong feature at 1.7 Å. This distance matches the main EXAFS feature for the reference PtO_2, suggesting the R5 template may be inhibiting Pt reduction. This is likely due to the low reduction potential of Pt^{2+} ions when complexed to amines, where it is thought to depend on the initial Pt seed formation during particle synthesis.[59] If a zerovalent Pt seed is formed, then nucleation of the Pt particle is rapid, but if no Pt seed forms, the Pt^{2+} is trapped within the template in its oxidized form.[59] Similar results have been previously observed by Borodko et al.[60] in dendrimer systems. In that work, they indicated that interactions between amines in the dendrimer and Pt^{2+} ions resulted in a shifting of the Pt reduction potential to be more negative, thus making it more difficult to reduce with $NaBH_4$.[60] This oxide feature is notable in the EXAFS for $Pd_{25}Pt_{75}$, $Pd_{33}Pt_{67}$, and $Pd_{50}Pt_{50}$ and minimally in $Pd_{67}Pt_{33}$, while metal−metal features shift toward longer real-space distances with increasing Pt content.

To obtain quantitative atomic-scale structural information, Pd and Pt EXAFS were modeled by use of FEFF6 theory[52] to obtained element-specific coordination numbers (CNs) and

DOI: 10.1021/acsami.6b11651
ACS Appl. Mater. Interfaces 2017, 9, 8030−8040

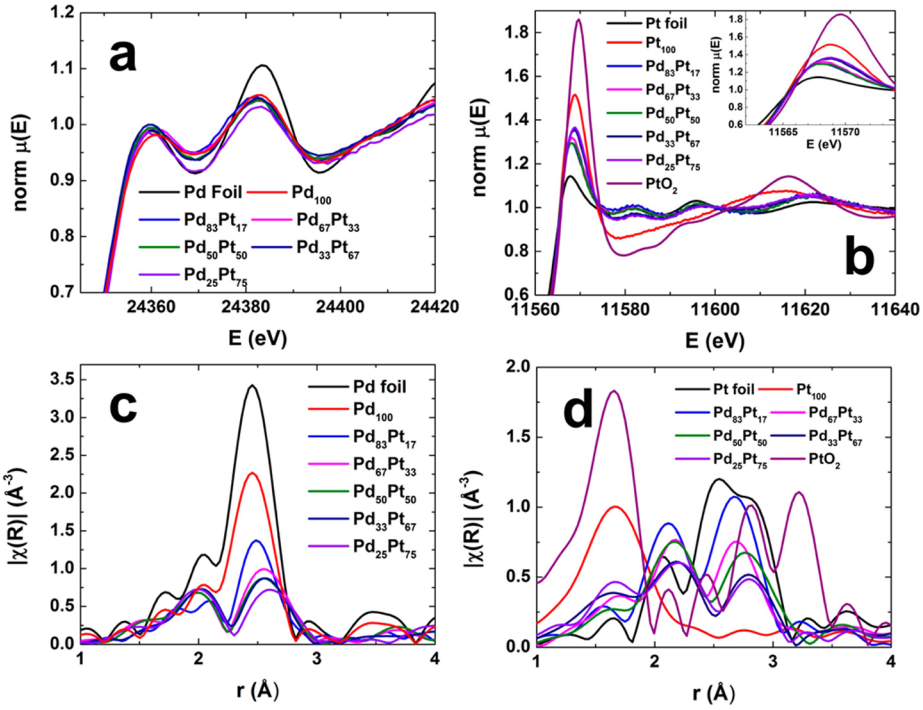

Figure 4. XAFS analysis of RS-templated PdPt bimetallic materials. (a, b) XANES data at (a) Pd K edge and (b) Pt L_3 edge. (Inset) Changes in white line intensity. (c, d) EXAFS *r*-space data at (c) Pd K edge and (d) Pt L_3 edge.

Table 1. Calculated Coordination Numbers from EXAFS Modeling of both Pd K-edge and Pt L_3-edge Data Sets

	CN				
	Pd−Pd	Pd−Pt	Pt−Pt	Pt−Pd	Pt−Cl/O
Pd_{100}	7.5 ± 0.5				
$Pd_{83}Pt_{17}$	5.6 ± 0.9	1.1 ± 1.5		6.7 ± 2.0	0.3 ± 0.5 (Cl)
$Pd_{67}Pt_{33}$	5.5 ± 0.8	1.7 ± 0.8	3.2 ± 3.2	5.0 ± 4.3	1.1 ± 1.5 (Cl)
$Pd_{50}Pt_{50}$	4.8 ± 0.7	3.5 ± 0.6	5.1 ± 1.2	3.5 ± 0.6	0.2 ± 0.5 (O)
$Pd_{33}Pt_{67}$	3.6 ± 0.5	5.7 ± 0.4	4.9 ± 1.5	2.8 ± 0.4	0.9 ± 0.8 (O)
$Pd_{25}Pt_{75}$	3.3 ± 0.6	5.8 ± 0.4	5.5 ± 1.2	1.9 ± 0.4	0.8 ± 0.4 (O)
Pt_{100}					0.8 ± 0.3 (Cl)
					3.3 ± 0.6 (O)

bond lengths. (See Supporting Information Figures S1 and S2 for Pd K edge and Pt L_3 edge fits, respectively.) The resulting CNs are summarized in Table 1 and Figure 5, with the remaining metrics summarized in the Table S1 in Supporting Information. For the Pt_{100} nanomaterials, the EXAFS data suggested that no metallic Pt character was present in the sample (Figure 4d). Modeling the Pt_{100} EXAFS data confirms the strong presence of unreduced species in this material with the best fit resulting in a Pt−Cl CN of 0.8 ± 0.3 and a Pt−O/N CN of 3.3 ± 0.6. For the $Pd_{25}Pt_{75}$, $Pd_{33}Pt_{67}$, and $Pd_{50}Pt_{50}$ nanomaterials, Pt − low-*Z* contributors can be observed in the Pt EXAFS (Figure 4d), which were successfully modeled with Pt−O instead of Pt−Cl contributions. The nucleation of Pd generated metal seeds within the peptide template to facilitate the reduction of $PtCl_4^{2-}$, eliminating the Pt−Cl species. Once reduced, the Pt subsequently oxidizes, however, as indicated from EXAFS modeling efforts. The heterogeneity of the Pt species arises from the presence of reduced Pt^0, oxidized Pt−O, and unreduced K_2PtCl_4, which substantially complicates structural analysis based on CNs, as XAFS is a bulk measurement reflecting the ensemble-average Pt environment in the sample. Such overall Pt−Pt and Pt−Pd CNs were converted into effective CNs accounting only for the nanoparticle phase, thus enabling modeling of structure and composition of the nanoparticles.[61] With $PtCl_4^{2-}$ having a Pt−Cl CN of 4.0, the best-fit result for the Pt−Cl CN can be used

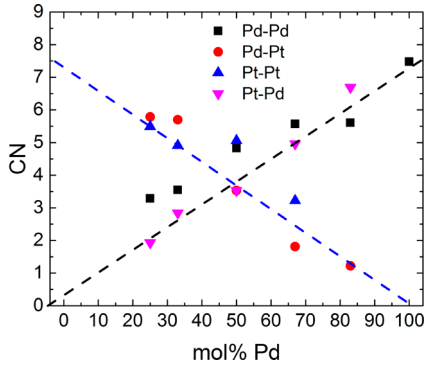

Figure 5. Effective CNs for PdPt bimetallic nanomaterials vs Pd composition. The dashed black line represents Pd−Pd CN trend vs composition for a random nanoalloy alloy, while the dashed blue line represent the analogous trend for Pt−Pt.

DOI: 10.1021/acsami.6b11651
ACS Appl. Mater. Interfaces 2017, 9, 8030−8040

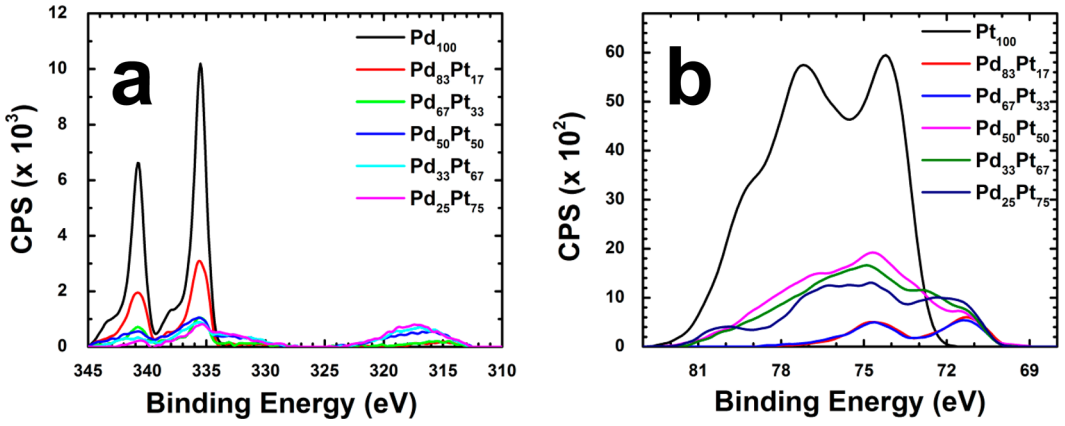

Figure 6. High-resolution XPS spectra of PdPt materials: (a) Pd 3d with interference from Pt 4d and (b) Pt 4f.

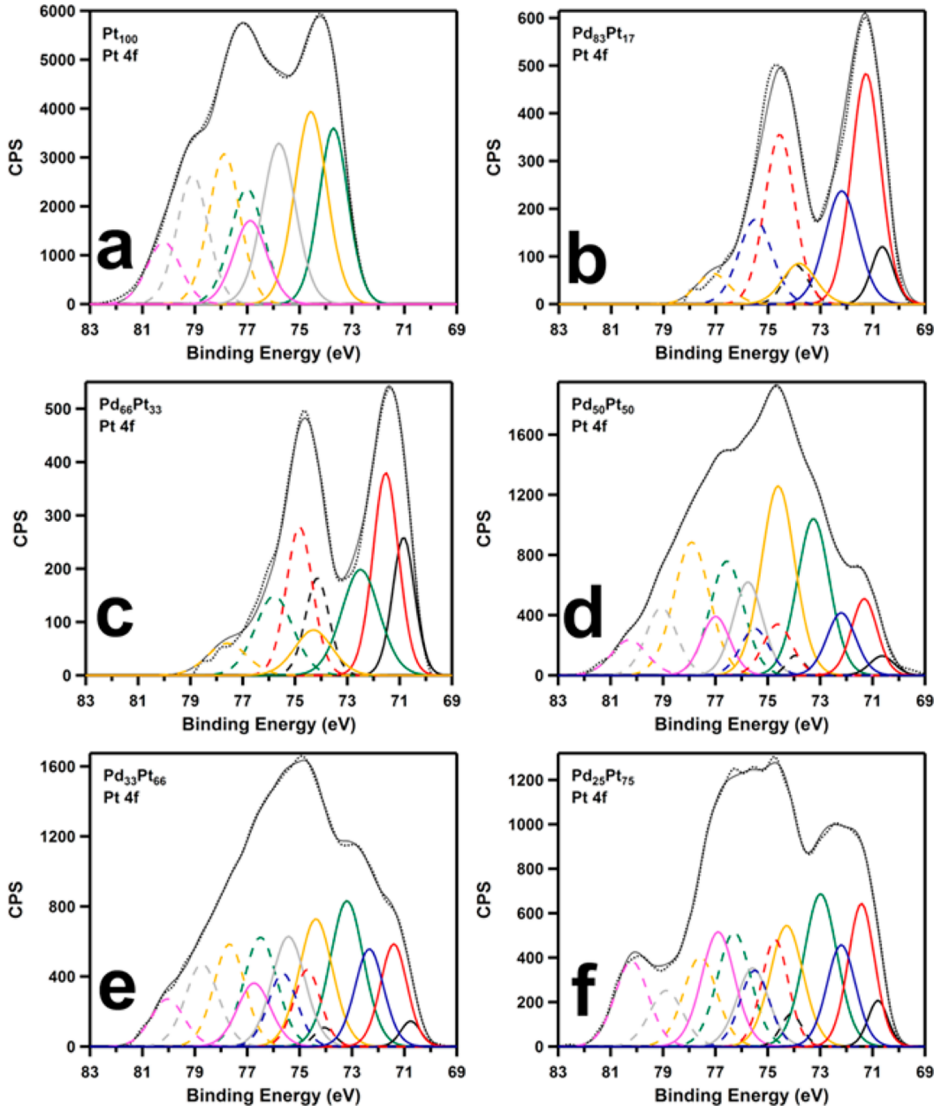

Figure 7. Curve-fitted high-resolution Pt 4f XPS spectra for (a) Pt_{100}, (b) $Pd_{83}Pt_{17}$, (c) $Pd_{66}Pt_{33}$, (d) $Pd_{50}Pt_{50}$, (e) $Pd_{33}Pt_{66}$, and (f) $Pd_{25}Pt_{75}$ samples. Representative high-resolution Pt 4f spectra were fitted with seven peaks, each consisting of two components, 4f7/2 (solid lines) and 4f5/2 (dashed lines), separated by 3.3 eV.

to assess the amount of unreduced Pt and, subsequently, modify the nanoparticle CN (see ref 61 for details). By examining the effective CNs for $Pd_{67}Pt_{33}$ and $Pd_{83}Pt_{17}$, we conclude that the nanomaterials are largely alloyed because the effective CNs trend linearly with composition, as anticipated for random alloys (Figure 5).[61]

The EXAFS data analysis provides significant information concerning the structure of the materials at the atomic level.

DOI: 10.1021/acsami.6b11651
ACS Appl. Mater. Interfaces 2017, 9, 8030−8040

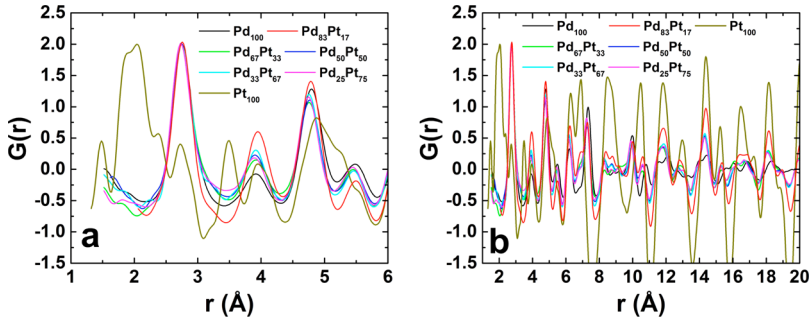

Figure 8. PDFs for R5-templated PdPt materials up to (a) 6 Å and (b) 20 Å to illustrate structural differences at various length scales.

Taken together, the XAFS data indicate that the Pd regions are largely metallic in nature and do not exhibit any significant Pd−ligand interactions. This suggests minimal degrees of interaction between the Pd metal and the peptide template. Conversely, the Pt atoms display Pd-dependent levels of oxidization for materials with a composition of <50% Pd. In general, these Pt-based oxide materials are likely to be deposited on the particle surface due to the slower kinetics of Pt^{2+} reduction due to coordination with amines in the R5 template.[59] Overall, the PdPt nanoparticles exhibited largely linear CN behavior with respect to composition (Figure 5), conforming to the anticipated values for an alloyed PdPt structure. Similar results were found for R5-templated PdAu,[10] indicating that the R5 template is capable of facilitating the fabrication of alloyed nanomaterials.

To complement and support the EXAFS results, XPS was performed on the bimetallic materials to further probe the composition and arrangement of the nanostructures, with particular attention paid to the metal atom oxidation state. High-resolution Pd 3d XPS spectra (Figure 6a) indicate that Pd is very similar chemically for Pd_{100} and all R5-templated multicomponent nanomaterials. The peaks at 335.8 eV are due to zerovalent Pd, while a small shoulder at 338 eV, found in nanomaterials with higher Pd content, is likely due to small amounts of oxidation. In nanomaterials with high Pt content, strong Pt 4d peaks observed at 317 and 334 eV interfere with the Pd 3d peaks, making it difficult to quantify the Pd species. High-resolution Pt 4f spectra (Figure 6b) indicate significant oxidization of Pt in the R5-templated materials. Peaks with deconvoluted features at 70.8, 71.4, 72.3, 73.2, 74.4, 75.4, and 76.7 are observed (Figure 7). The peaks at 73.2 and 74.4 eV indicate the presence of potassium chloroplatinates, originating from the precursor compound, and may also indicate the formation of PtO_2 and/or $Pt(OH)_4$, which are likely to arise from incomplete Pt reduction within the R5 template.[62,63] The peak at 76.7 suggests that a significant amount of Pt is coordinated to the peptide template. Peaks at lower binding energy indicate the presence of metallic Pt (70.8 and 71.4 eV) and PtO (72.3 eV). As the amount of Pd increases in the multicomponent materials, the Pt features due to the reduced forms become more observable. For instance, $Pd_{25}Pt_{75}$, and $Pd_{33}Pt_{67}$ begin to exhibit peaks at 71.4 eV for zerovalent Pt but still have extensive oxidation features similar to those observed in Pt_{100}. At equimolar Pd and Pt concentrations, metallic Pt becomes more predominant but still with notable amounts of oxidation, while $Pd_{67}Pt_{33}$ and $Pd_{83}Pt_{17}$ appear to be primarily metallic for both Pd and Pt with very limited oxidation. Taken together, the XPS data corroborate the EXAFS findings that R5-templated nanomaterials create Pd-dependent Pt oxidation when synthesized under aqueous conditions.

From the EXAFS and XPS analyses, clear atomic-scale structural and chemical differences are observed, which likely depend on both the bimetallic composition and metal atom interactions with the templating peptide. To further probe the intricate material morphology, HE-XRD coupled to atomic PDF analysis was also conducted to determine the structural arrangement of Pd and Pt at length scales larger than the first coordination sphere. PDF analysis is advantageous for materials lacking long-range structural order, such as nanomaterials, as both Bragg peaks (from crystalline domains) and diffuse scattering (arising from a lack of long-range periodicity) are accounted for in the analysis.[64] HE-XRD patterns of high statistical quality are collected to high reciprocal space vectors (~45 $Å^{-1}$), converted into total structure functions $F(Q)$ (see Supporting Information Figures S3 and S4), and then Fourier-transformed into atomic PDFs that provide subangstrom structural information on the size of the nanomaterials. PDFs for the R5-templated PdPt nanomaterials are shown in Figure 8 up to 6 Å and 20 Å (data up to 40 Å are given in Supporting Information Figure S5).

The PDFs clearly indicate that the majority of Pt in Pt_{100} is not reduced, which exhibits Pt − low-Z peaks at 1.9 and 2.0 Å. These distances may be due to possible oxidation of Pt to oxides or hydroxides,[65,66] Pt^{2+}−peptide interactions, or Pt−Cl bonds from unreduced precursor as indicated from the EXAFS modeling (Figure 5 and Table 1). A minimal feature at 2.74 Å is likely due to the small fraction of zerovalent Pt nanomaterials not detectable with XAFS but observed by TEM. Additional longer-range PDF features are found at positions for face-centered cubic (fcc)-type arrangement of atoms are also observed, although the dominant presence of unreduced Pt complicates further analysis. Note that the aforementioned low-Z features are not present in the bimetallic nanomaterials. This indicates that any oxidized Pt is likely on the surface of the nanomaterial, as it does not have a strong peak in the atomic PDF, due to the comparatively smaller number of Pt − low-Z atomic pairs and high contrast between O and Pt/Pd. As PDF analysis is based on diffraction data, it is not as sensitive to low-Z surface structures as spectroscopic methods such as XPS or EXAFS. Similarly, small amounts of unreduced Pt likely will not exhibit features in the PDF for $Pd_{83}Pt_{17}$ and $Pd_{67}Pt_{33}$ due to overall small contributions to the HE-XRD that are largely neglected upon Fourier transformation to the atomic PDF.[25] The dampening in peak oscillations between Pt_{100} and the bimetallic nanomaterials further indicates substantial oxidation in Pt_{100}. The alloyed nanomaterials exhibit dampened pair distances in relative magnitude at larger real-space distances,

DOI: 10.1021/acsami.6b11651
ACS Appl. Mater. Interfaces 2017, 9, 8030−8040

which is indicative of metallic bonding observed from the structure-sensitive PDFs. Conversely, Pt_{100} exhibits a PDF that lacks peak dampening at larger real-space distances, suggesting the presence of a high degree of covalent bonding that would be present in an oxidized material. The R5-templated PdPt structures exhibit various changes in both peak position and peak broadening that are not strictly dependent on the Pd:Pt ratio. This would suggest that the atomic-scale structure of these materials is likely dependent on the interplay between multicomponent material stoichiometry and subsequent Pt reduction/oxidation, along with interaction between the inorganic and biological components.[25,26]

From the suite of X-ray characterization methods, we hypothesize that Pd and Pt are largely alloyed within the R5 template, with quantifiable amounts of Pt oxidation due to the inability to fully reduce Pt for materials with higher Pt loading (Scheme 1). In these materials, the Pd atoms likely are reduced

Scheme 1. Mechanism for Formation of PdPt Materials Employing the R5 Template

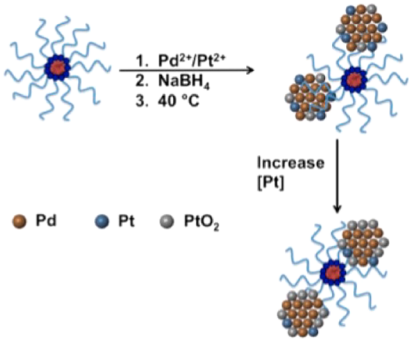

first upon addition of $NaBH_4$, followed by the incorporation of metallic Pt, which can become partially oxidized at the surface. Upon incorporation of reduced Pt, bimetallic nanoparticles are generated in an alloyed-like structure, which has been demonstrated to be relatively stable in previous reports.[67−69] The extent of Pt oxidation and metallic Pt incorporation into the nanomaterials is dependent on the amount of Pd in the sample, controlled by the Pd:Pt ratio. Pd-dependent oxidation of Pt is likely due to enhanced reduction of Pt^{2+} facilitated by the generation of Pd seeds in this sample, coupled with a shift in Pt^{2+} reduction potential due to interactions with the biotemplate. Since the oxidized materials were not observed in the PDFs but were noted by EXAFS and XPS, the oxidized Pt is more likely to be prevalent at the material surface, wherein diffraction methods are limited at resolving low-Z surface materials. At higher Pd:Pt ratios, Pt oxidation is minimal, with EXAFS modeling confirming metallic Pt atoms incorporated throughout the nanomaterial. Understanding the interplay between Pd and Pt reduction due to reaction stoichiometry and peptide−precursor interactions can assist in understanding the properties of these materials and can be further extended to other bimetallic nanomaterial combinations templated by biological macromolecules.

Once the structure of the nanomaterials was more fully understood, their catalytic activity was tested by use of hydrogenation of olefins as a model reaction (Figure 9). To determine the effects of olefin structure on reactivity, primary, secondary, and tertiary alcohols were used as substrates. For this, allyl alcohol, 3-buten-2-ol, and 2-methyl-3-buten-2-ol were

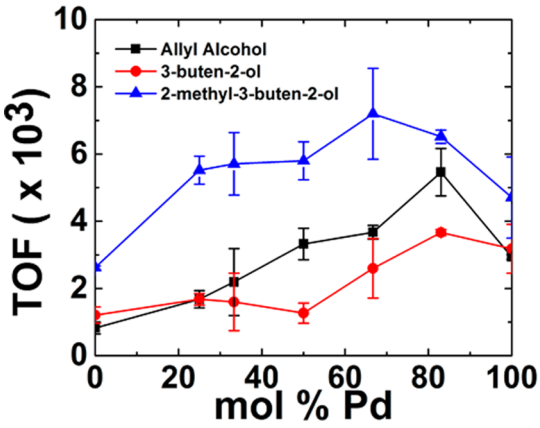

Figure 9. TOF plots of R5-templated PdPt materials for the olefin hydrogenation of allyl alcohol (black), 3-buten-2-ol (red), and 2-methyl-3-buten-2-ol (blue).

employed, respectively. We have previously reported catalytic TOFs for monometallic R5-templated Pd and Pt where moderately high values were observed for the Pd materials [~2900 mol product (mol metal × h)$^{-1}$] and significantly lower average TOFs were noted for the Pt materials [~792 mol product (mol metal × h)$^{-1}$].[2] Figure 9 presents the catalytic TOF values for the bimetallic nanomaterials on the primary, secondary, or tertiary alcohol, where an increase in reactivity was observed for certain ratios of Pd:Pt. For hydrogenation of the primary alcohol, allyl alcohol, a TOF of 2937 ± 73 mol product (mol metal × h)$^{-1}$ was determined for the Pd_{100} material, consistent with previous results.[2,50] Upon the addition of a small amount (17%) of Pt, an enhancement in the TOF to 5459 ± 705 mol product (mol metal × h)$^{-1}$ was observed for the $Pd_{83}Pt_{17}$ material. With further increases in Pt concentration, a steady decrease in the TOF was observed, with values of 3671 ± 206, 3322 ± 470, 2190 ± 998, 1677 ± 257, and 825 ± 177 mol product (mol metal × h)$^{-1}$ for $Pd_{67}Pt_{33}$, $Pd_{50}Pt_{50}$, $Pd_{33}Pt_{67}$, $Pd_{25}Pt_{75}$, and Pt_{100} materials, respectively. Such an effect of diminished reactivity was anticipated, as unreduced or oxidized Pt are anticipated to have lower reactivity compared to Pd. Note that these TOF values for all materials that possess Pd have greater reactivity as compared to a standard Pd-on-carbon material that previously demonstrated a TOF of 1059 ± 127 mol product (mol metal × h)$^{-1}$ for hydrogenation of allyl alcohol under identical conditions.[2]

For the $Pd_{83}Pt_{17}$ material, recyclability of the nanocatalysts for hydrogenation of allyl alcohol was studied (Supporting Information, Figure S6). These structures were specifically chosen as they demonstrated the maximum reactivity based upon TOF values. Unfortunately, after subsequent reaction cycles, the observed TOF values generally decreased. To this end, the materials initially demonstrated a TOF value of 5565 ± 917 mol product (mol metal × h)$^{-1}$ for the first reaction, which decreased to 1655 ± 408 mol product (mol metal × h)$^{-1}$ after four reaction cycles. Such a lack of recyclability may be due to instability of the peptide template or aggregation of materials. Increasing the recyclability of the material's reactivity could be achieved via enhanced peptide template stability and increasing the charge on the materials (leading to enhanced electrostatic-based stability of the materials); however, the key result of a bimetallic effect for enhanced reactivity was maintained for the initial catalytic cycles with the PdPt-containing nanocatalysts.

DOI: 10.1021/acsami.6b11651
ACS Appl. Mater. Interfaces 2017, 9, 8030−8040

The size and structure of the substrate can also play a role in reactivity of nanomaterials.[50] To determine how this affects the peptide-templated bimetallic nanomaterials, secondary and tertiary olefinic alcohols 3-buten-2-ol and 2-methyl-3-buten-2-ol, respectively, were studied. Similar trends were observed for each substrate as compared to the primary alcohol, where an increased TOF was noted for the $Pd_{83}Pt_{17}$ materials, as compared to the Pd_{100} structures. For 3-buten-2-ol, a TOF of 3182 ± 727 mol product (mol metal × h)$^{-1}$ was determined for Pd_{100}. A slight enhancement in catalytic activity was observed for $Pd_{83}Pt_{17}$ with a TOF of 3667 ± 91 mol product (mol metal × h)$^{-1}$. Further increasing Pt concentrations lead to a steady decline in TOF of 2598 ± 885 and 1266 ± 298 mol product (mol metal × h)$^{-1}$ for $Pd_{67}Pt_{33}$ and $Pd_{50}Pt_{50}$, respectively. A negligible change in TOF was determined for $Pd_{33}Pt_{67}$ and $Pd_{25}Pt_{75}$ samples before a TOF of 1208 ± 241 mol product (mol metal × h)$^{-1}$ was observed for the Pt_{100} nanomaterials. A slightly different trend was found for the tertiary alcohol, where a TOF of 4707 ± 1206 mol product (mol metal × h)$^{-1}$ was observed for Pd_{100}. The reactivity increased to 6515 ± 195 and 7197 ± 1353 mol product (mol metal × h)$^{-1}$ for the $Pd_{83}Pt_{17}$ and $Pd_{67}Pt_{33}$ materials, respectively, followed by a steady decline in reactivity for the remaining samples.

Overall, such trends were anticipated for catalytic reactivity of the peptide-templated PdPt nanomaterials. For all reaction substrates, notable increases were observed when the Pd_{100} samples were compared with those that contained small amounts of Pt. In these alloyed materials, the X-ray data indicated that the majority of the Pt was reduced, making the materials mostly bimetallic in nature. PdPt bimetallic particles are known to possess enhanced hydrogenation reactivity as compared to monometallic Pd nanomaterials due to electronic effects.[55] Such effects arise from the more electronegative Pt component pulling electron density from the Pd component, making the Pd more reactive for olefin hydrogenation. As the amount of Pt in the sample increased where oxide formation was noted, the reactivity diminished for all samples. This effect was anticipated as the metallic components were buried within a surface shell of oxidized Pt, thus sequestering the most reactive materials from the reaction substrates. Furthermore, Pt is less reactive for olefin hydrogenation as compared to Pd, thus aiding in the diminishment in reactivity that was observed.

CONCLUSIONS

In summary, PdPt nanomaterials were synthesized by use of R5 peptide template, where the arrangement of the two components in the composite structure was fully elucidated by atomic-scale structural methods. These materials were used for the hydrogenation of olefinic alcohols, demonstrating changes in reactivity correlating to the material composition. The multicomponent nanomaterials were nearly monodisperse and spherical across the various Pd:Pt ratios, where the size varied with metal composition. X-ray methods including XAFS, HE-XRD, and XPS were used to characterize the materials where Pt was highly oxidized at increased Pt concentrations. Catalytic enhancement was observed for materials with less than 25% Pt, which likely arose from synergistic effects between the two inorganic components. Such results demonstrate that unanticipated multicomponent materials can be generated via biomimetic approaches, where the interactions of the template can direct the formation of these unique structures. Such results could be exploited to generate complex multicomponent inorganic nanostructures for specific applications that require a close integration between multiple metallic compositions, as well as the inclusion of metal oxide components.

ASSOCIATED CONTENT

Supporting Information

The Supporting Information is available free of charge on the ACS Publications website at DOI: 10.1021/acsami.6b11651.

One table and seven figures showing complete EXAFS fitting analysis, HE-XRD and $F(Q)$ for PdPt materials, atomic PDF for PdPt particles out to 40 Å, catalytic recyclability analysis, and TEM size distribution histograms (PDF)

AUTHOR INFORMATION

Corresponding Authors

*(A.I.F.) E-mail anatoly.frenkel@stonybrook.edu.
*(N.M.B.) E-mail nicholas.bedford.ctr@us.af.mil.
*(M.R.K.) E-mail knecht@miami.edu.

ORCID

Tadeusz T. Nitka: 0000-0001-9435-6515
Anatoly I. Frenkel: 0000-0002-5451-1207
Marc R. Knecht: 0000-0002-7614-7258

Funding

This work was partially supportedby the National Science Foundation (M.R.K.: DMR-1145175). N.M.B. acknowledges fellowship support from a National Research Council associateship award during the initial phases of this work. A.I.F. acknowledges funding by the Division of Chemical Sciences, Geosciences, and Biosciences within the U.S. Department of Energy Office of Basic Energy Sciences, Grant DE-FG02-03ER15476. Use of the Advanced Photon Source, an Office of Science User Facility operated for the U.S. Department of Energy (DOE) Office of Science by Argonne National Laboratory, was supported by the U.S. DOE under Contract DE-AC02-06CH11357.

Notes

The authors declare no competing financial interest.

REFERENCES

(1) Bhandari, R.; Knecht, M. R. Effects of the Material Structure on the Catalytic Activity of Peptide-Templated Pd Nanomaterials. *ACS Catal.* **2011**, *1*, 89−98.

(2) Bhandari, R.; Pacardo, D. B.; Bedford, N. M.; Naik, R. R.; Knecht, M. R. Structural Control and Catalytic Reactivity of Peptide-Templated Pd and Pt Nanomaterials for Olefin Hydrogenation. *J. Phys. Chem. C* **2013**, *117*, 18053−18062.

(3) Yang, J.; Yang, J.; Ying, J. Y. Morphology and Lateral Strain Control of Pt Nanoparticles via Core−Shell Construction Using Alloy AgPd Core Toward Oxygen Reduction Reaction. *ACS Nano* **2012**, *6*, 9373−9382.

(4) Coppage, R.; Slocik, J. M.; Sethi, M.; Pacardo, D. B.; Naik, R. R.; Knecht, M. R. Elucidation of Peptide Effects that Control the Activity of Nanoparticles. *Angew. Chem., Int. Ed.* **2010**, *49*, 3767−3770.

(5) Briggs, B. D.; Knecht, M. R. Nanotechnology Meets Biology: Peptide-based Methods for the Fabrication of Functional Materials. *J. Phys. Chem. Lett.* **2012**, *3*, 405−418.

(6) Bhattacharjee, S.; Bruening, M. L. Selective Hydrogenation of Monosubstituted Alkenes by Pd Nanoparticles Embedded in Polyelectrolyte Films. *Langmuir* **2008**, *24*, 2916−2920.

(7) Bedford, N. M.; Bhandari, R.; Slocik, J. M.; Seifert, S.; Naik, R. R.; Knecht, M. R. Peptide-Modified Dendrimers as Templates for the Production of Highly Reactive Catalytic Nanomaterials. *Chem. Mater.* **2014**, *26*, 4082−4091.

DOI: 10.1021/acsami.6b11651
ACS Appl. Mater. Interfaces 2017, 9, 8030−8040

(8) Garcia-Martinez, J. C.; Lezutekong, R.; Crooks, R. M. Dendrimer-Encapsulated Pd Nanoparticles as Aqueous, Room-Temperature Catalysts for the Stille Reaction. *J. Am. Chem. Soc.* **2005**, *127*, 5097−5103.
(9) Jakhmola, A.; Bhandari, R.; Pacardo, D. B.; Knecht, M. R. Peptide Template Effects for the Synthesis and Catalytic Application of Pd Nanoparticle Networks. *J. Mater. Chem.* **2010**, *20*, 1522−1531.
(10) Merrill, N. A.; McKee, E. M.; Merino, K. C.; Drummy, L. F.; Lee, S.; Reinhart, B.; Ren, Y.; Frenkel, A. I.; Naik, R. R.; Bedford, N. M.; Knecht, M. R. Identifying the Atomic-Level Effects of Metal Composition on the Structure and Catalytic Activity of Peptide-Templated Materials. *ACS Nano* **2015**, *9*, 11968−11979.
(11) Scott, R. W. J.; Wilson, O. M.; Oh, S.-K.; Kenik, E. A.; Crooks, R. M. Bimetallic Palladium−Gold Dendrimer-Encapsulated Catalysts. *J. Am. Chem. Soc.* **2004**, *126*, 15583−15591.
(12) El-Deab, M. S.; Ohsaka, T. Manganese Oxide Nanoparticles Electrodeposited on Platinum Are Superior to Platinum for Oxygen Reduction. *Angew. Chem., Int. Ed.* **2006**, *45*, 5963−5966.
(13) Wang, C.; Yin, H.; Dai, S.; Sun, S. A General Approach to Noble Metal−Metal Oxide Dumbbell Nanoparticles and Their Catalytic Application for CO Oxidation. *Chem. Mater.* **2010**, *22*, 3277−3282.
(14) Shiraishi, Y.; Fujiwara, K.; Sugano, Y.; Ichikawa, S.; Hirai, T. N-Monoalkylation of Amines with Alcohols by Tandem Photocatalytic and Catalytic Reactions on TiO_2 Loaded with Pd Nanoparticles. *ACS Catal.* **2013**, *3*, 312−320.
(15) Tao, F. Synthesis, Catalysis, Surface Chemistry and Structure of Bimetallic Nanocatalysts. *Chem. Soc. Rev.* **2012**, *41*, 7977−7979.
(16) Misch, L. M.; Kurzman, J. A.; Derk, A. R.; Kim, Y.-I.; Seshadri, R.; Metiu, H.; McFarland, E. W.; Stucky, G. D. C−H Bond Activation by Pd-substituted CeO_2: Substituted Ions versus Reduced Species. *Chem. Mater.* **2011**, *23*, 5432−5439.
(17) Yu, H.; Chen, M.; Rice, P. M.; Wang, S. X.; White, R. L.; Sun, S. Dumbbell-like Bifunctional Au−Fe_3O_4 Nanoparticles. *Nano Lett.* **2005**, *5*, 379−382.
(18) Frey, N. A.; Phan, M. H.; Srikanth, H.; Srinath, S.; Wang, C.; Sun, S. Interparticle interactions in coupled Au−Fe_3O_4 nanoparticles. *J. Appl. Phys.* **2009**, *105*, No. 07B502.
(19) Weiss, W.; Ritter, M. Metal oxide heteroepitaxy: Stranski-Krastanov Growth for Iron Oxides on Pt(111). *Phys. Rev. B: Condens. Matter Mater. Phys.* **1999**, *59*, 5201−5213.
(20) Gilbert, B.; Huang, F.; Zhang, H.; Waychunas, G. A.; Banfield, J. F. Nanoparticles: Strained and Stiff. *Science* **2004**, *305*, 651−654.
(21) Huang, W. J.; Sun, R.; Tao, J.; Menard, L. D.; Nuzzo, R. G.; Zuo, J. M. Coordination-Dependent Surface Atomic Contraction in Nanocrystals Revealed by Coherent Diffraction. *Nat. Mater.* **2008**, *7*, 308−313.
(22) Dash, P.; Bond, T.; Fowler, C.; Hou, W.; Coombs, N.; Scott, R. W. J. Rational Design of Supported PdAu Nanoparticle Catalysts from Structured Nanoparticle Precursors. *J. Phys. Chem. C* **2009**, *113*, 12719−12730.
(23) Bedford, N.; Dablemont, C.; Viau, G.; Chupas, P.; Petkov, V. 3-D Structure of Nanosized Catalysts by High-Energy X-ray Diffraction and Reverse Monte Carlo Simulations: Study of Ru. *J. Phys. Chem. C* **2007**, *111*, 18214−18219.
(24) Tang, Z.; Palafox-Hernandez, J. P.; Law, W.-C.; Hughes, Z. E.; Swihart, M. T.; Prasad, P. N.; Knecht, M. R.; Walsh, T. R. Biomolecular Recognition Principles for Bionanocombinatorics: An Integrated Approach To Elucidate Enthalpic and Entropic Factors. *ACS Nano* **2013**, *7*, 9632−9646.
(25) Bedford, N. M.; Ramezani-Dakhel, H.; Slocik, J. M.; Briggs, B. D.; Ren, Y.; Frenkel, A. I.; Petkov, V.; Heinz, H.; Naik, R. R.; Knecht, M. R. Elucidation of Peptide-Directed Palladium Surface Structure for Biologically Tunable Nanocatalysts. *ACS Nano* **2015**, *9*, 5082−5092.
(26) Bedford, N. M.; Hughes, Z. E.; Tang, Z.; Li, Y.; Briggs, B. D.; Ren, Y.; Swihart, M. T.; Petkov, V. G.; Naik, R. R.; Knecht, M. R.; Walsh, T. R. Sequence-Dependent Structure/Function Relationships of Catalytic Peptide-Enabled Gold Nanoparticles Generated under Ambient Synthetic Conditions. *J. Am. Chem. Soc.* **2016**, *138*, 540−548.
(27) Graf, P.; Mantion, A.; Haase, A.; Thünemann, A. F.; Mašić, A.; Meier, W.; Luch, A.; Taubert, A. Silicification of Peptide-Coated Silver Nanoparticles—A Biomimetic Soft Chemistry Approach toward Chiral Hybrid Core−Shell Materials. *ACS Nano* **2011**, *5*, 820−833.
(28) Oh, D.; Qi, J.; Han, B.; Zhang, G.; Carney, T. J.; Ohmura, J.; Zhang, Y.; Shao-Horn, Y.; Belcher, A. M. M13 Virus-Directed Synthesis of Nanostructured Metal Oxides for Lithium−Oxygen Batteries. *Nano Lett.* **2014**, *14*, 4837−4845.
(29) Nuraje, N.; Lei, Y.; Belcher, A. Virus-Templated Visible Spectrum Active Perovskite Photocatalyst. *Catal. Commun.* **2014**, *44*, 68−72.
(30) Courchesne, N.-M. D.; Klug, M. T.; Chen, P.-Y.; Kooi, S. E.; Yun, D. S.; Hong, N.; Fang, N. X.; Belcher, A. M.; Hammond, P. T. Assembly of a Bacteriophage-Based Template for the Organization of Materials into Nanoporous Networks. *Adv. Mater.* **2014**, *26*, 3398−3404.
(31) Mao, C.; Flynn, C. E.; Hayhurst, A.; Sweeney, R.; Qi, J.; Georgiou, G.; Iverson, B.; Belcher, A. M. Viral Assembly of Oriented Quantum Dot Nanowires. *Proc. Natl. Acad. Sci. U. S. A.* **2003**, *100*, 6946−6951.
(32) Qin, L.-X.; Li, Y.; Li, D.-W.; Jing, C.; Chen, B.-Q.; Ma, W.; Heyman, A.; Shoseyov, O.; Willner, I.; Tian, H.; Long, Y.-T. Electrodeposition of Single-Metal Nanoparticles on Stable Protein1-Membranes: Application of Plasmonic Sensing by Single Nanoparticles. *Angew. Chem., Int. Ed.* **2012**, *51*, 140−144.
(33) Klem, M. T.; Mosolf, J.; Young, M.; Douglas, T. Photochemical Mineralization of Europium, Titanium, and Iron Oxyhydroxide Nanoparticles in the Ferritin Protein Cage. *Inorg. Chem.* **2008**, *47*, 2237−2239; Correction. **2009**, *48*, 9041 DOI: 10.1021/ic901346s.
(34) Sadasivan, S.; Patil, A. J.; Bromley, K. M.; Hastie, P. G. R.; Banting, G.; Mann, S. Novel Protein-Inorganic Nanoparticles Prepared by Inorganic Replication of Self-Assembled Clathrin Cages and Triskelia. *Soft Matter* **2008**, *4*, 2054−2058.
(35) Fang, Y.; Wu, Q.; Dickerson, M. B.; Cai, Y.; Shian, S.; Berrigan, J. D.; Poulsen, N.; Kröger, N.; Sandhage, K. H. Protein-Mediated Layer-by-Layer Syntheses of Freestanding Microscale Titania Structures with Biologically Assembled 3-D Morphologies. *Chem. Mater.* **2009**, *21*, 5704−5710.
(36) Huggins, K. N. L.; Schoen, A. P.; Arunagirinathan, M. A.; Heilshorn, S. C. Multi-Site Functionalization of Protein Scaffolds for Bimetallic Nanoparticle Templating. *Adv. Funct. Mater.* **2014**, *24*, 7737−7744.
(37) Schoen, A. P.; Huggins, K. N. L.; Heilshorn, S. C. Engineered Clathrin Nanoreactors Provide Tunable Control over Gold Nanoparticle Synthesis and Clustering. *J. Mater. Chem. B* **2013**, *1*, 6662−6669.
(38) Schoen, A. P.; Schoen, D. T.; Huggins, K. N. L.; Arunagirinathan, M. A.; Heilshorn, S. C. Template Engineering Through Epitope Recognition: A Modular, Biomimetic Strategy for Inorganic Nanomaterial Synthesis. *J. Am. Chem. Soc.* **2011**, *133*, 18202−18207.
(39) Chen, P.-Y.; Dang, X.; Klug, M. T.; Qi, J.; Dorval Courchesne, N.-M.; Burpo, F. J.; Fang, N.; Hammond, P. T.; Belcher, A. M. Versatile Three-Dimensional Virus-Based Template for Dye-Sensitized Solar Cells with Improved Electron Transport and Light Harvesting. *ACS Nano* **2013**, *7*, 6563−6574.
(40) Lee, S.-K.; Yun, D. S.; Belcher, A. M. Cobalt Ion Mediated Self-Assembly of Genetically Engineered Bacteriophage for Biomimetic Co−Pt Hybrid Material. *Biomacromolecules* **2006**, *7*, 14−17.
(41) Chen, P.-Y.; Dang, X.; Klug, M. T.; Courchesne, N.-M. D.; Qi, J.; Hyder, M. N.; Belcher, A. M.; Hammond, P. T. M13 Virus-Enabled Synthesis of Titanium Dioxide Nanowires for Tunable Mesoporous Semiconducting Networks. *Chem. Mater.* **2015**, *27*, 1531−1540.
(42) Kröger, N.; Lorenz, S.; Brunner, E.; Sumper, M. Self-Assembly of Highly Phosphorylated Silaffins and Their Function in Biosilica Morphogenesis. *Science* **2002**, *298*, 584−586.
(43) Poulsen, N.; Sumper, M.; Kröger, N. Biosilica Formation in Diatoms: Characterization of Native Silaffin-2 and its Role in Silica

DOI: 10.1021/acsami.6b11651
ACS Appl. Mater. Interfaces 2017, 9, 8030−8040

Morphogenesis. *Proc. Natl. Acad. Sci. U. S. A.* **2003**, *100*, 12075−12080.
(44) Bhandari, R.; Knecht, M. R. Isolation of Template Effects That Control the Structure and Function of Nonspherical, Biotemplated Pd Nanomaterials. *Langmuir* **2012**, *28*, 8110−8119.
(45) Bhandari, R.; Knecht, M. R. Synthesis, Characterization, and Catalytic Application of Networked Au Nanostructures Fabricated Using Peptide Templates. *Catal. Sci. Technol.* **2012**, *2*, 1360−1366.
(46) Li, Y.; Bastakoti, B. P.; Malgras, V.; Li, C.; Tang, J.; Kim, J. H.; Yamauchi, Y. Back Cover: Polymeric Micelle Assembly for the Smart Synthesis of Mesoporous Platinum Nanospheres with Tunable Pore Sizes. *Angew. Chem., Int. Ed.* **2015**, *54*, 11290−11290.
(47) Wang, L.; Yamauchi, Y. Metallic Nanocages: Synthesis of Bimetallic Pt−Pd Hollow Nanoparticles with Dendritic Shells by Selective Chemical Etching. *J. Am. Chem. Soc.* **2013**, *135*, 16762−16765.
(48) Malgras, V.; Ataee-Esfahani, H.; Wang, H.; Jiang, B.; Li, C.; Wu, K. C. W.; Kim, J. H.; Yamauchi, Y. Nanoarchitectures for Mesoporous Metals. *Adv. Mater.* **2016**, *28*, 993−1010.
(49) Chan, W. C., White, P. D. *Fmoc Solid Phase Peptide Synthesis: A Practical Approach*. Oxford University Press: New York, 2000.
(50) Pacardo, D. B.; Ardman, E.; Knecht, M. R. Effects of Substrate Molecular Structure on the Catalytic Activity of Peptide-Templated Pd Nanomaterials. *J. Phys. Chem. C* **2014**, *118*, 2518−2527.
(51) Petkov, V. *Rad*, A Program for Analysis of X-Ray-Diffraction Data from Amorphous Materials for Personal Computers. *J. Appl. Crystallogr.* **1989**, *22*, 387−389.
(52) Ravel, B.; Newville, M. ATHENA, ARTEMIS, HEPHAESTUS: Data Analysis for X-ray Absorption Spectroscopy Using IFEFFIT. *J. Synchrotron Radiat.* **2005**, *12*, 537−541.
(53) Vinodgopal, K.; He, Y.; Ashokkumar, M.; Grieser, F. Sonochemically Prepared Platinum−Ruthenium Bimetallic Nanoparticles. *J. Phys. Chem. B* **2006**, *110*, 3849−3852.
(54) Creighton, J. A.; Eadon, D. G. Ultraviolet-Visible Absorption Spectra of the Colloidal Metallic Elements. *J. Chem. Soc., Faraday Trans.* **1991**, *87*, 3881−3891.
(55) Scott, R. W. J.; Datye, A. K.; Crooks, R. M. Bimetallic Palladium−Platinum Dendrimer-Encapsulated Catalysts. *J. Am. Chem. Soc.* **2003**, *125*, 3708−3709.
(56) Lahiri, D.; Bunker, B.; Mishra, B.; Zhang, Z.; Meisel, D.; Doudna, C. M.; Bertino, M. F.; Blum, F. D.; Tokuhiro, A. T.; Chattopadhyay, S.; Shibata, T.; Terry, J. Bimetallic Pt−Ag and Pd−Ag nanoparticles. *J. Appl. Phys.* **2005**, *97*, No. 094304.
(57) Liu, F.; Wechsler, D.; Zhang, P. Alloy-Structure-Dependent Electronic Behavior and Surface Properties of Au−Pd Nanoparticles. *Chem. Phys. Lett.* **2008**, *461*, 254−259.
(58) Coppage, R.; Slocik, J. M.; Briggs, B. D.; Frenkel, A. I.; Naik, R. R.; Knecht, M. R. Determining Peptide Sequence Effects That Control the Size, Structure, and Function of Nanoparticles. *ACS Nano* **2012**, *6*, 1625−1636.
(59) Anderson, R. M.; Yancey, D. F.; Loussaert, J. A.; Crooks, R. M. Multistep Galvanic Exchange Synthesis Yielding Fully Reduced Pt Dendrimer-Encapsulated Nanoparticles. *Langmuir* **2014**, *30*, 15009−15015.
(60) Borodko, Y.; Thompson, C. M.; Huang, W.; Yildiz, H. B.; Frei, H.; Somorjai, G. A. Spectroscopic Study of Platinum and Rhodium Dendrimer (PAMAM G4OH) Compounds: Structure and Stability. *J. Phys. Chem. C* **2011**, *115*, 4757−4767.
(61) Frenkel, A. Solving the 3D structure of metal nanoparticles. *Z. Kristallogr. - Cryst. Mater.* **2007**, *222*, 605−611.
(62) Nefedov, V. I.; Salyn, Y. V.; Baranovski, I. B.; Majorova, A. G. *Zh. Neorg. Khim.* **1980**, *25*, 216.
(63) Fierro, J. L. G.; Palacios, J. M.; Tomas, F. An Analytical SEM and XPS Study of Platinum−Rhodium Gauzes used in High Pressure Ammonia Burners. *Surf. Interface Anal.* **1988**, *13*, 25−32.
(64) Petkov, V. Nanostructure by High-Energy X-ray Diffraction. *Mater. Today* **2008**, *11*, 28−38.
(65) Alayon, E. M. C.; Singh, J.; Nachtegaal, M.; Harfouche, M.; van Bokhoven, J. A. *In situ* XAS Probes Partially Oxidized Platinum Generating High Activity for CO Oxidation. *J. Phys. Conf. Ser.* **2009**, *190*, No. 012152.
(66) Park, K.-T.; Novikov, D. L.; Gubanov, V. A.; Freeman, A. J. Electronic Structure of Noble-Metal Monoxides: PdO, PtO, and AgO. *Phys. Rev. B: Condens. Matter Mater. Phys.* **1994**, *49*, 4425−4431.
(67) Wang, L.-L.; Johnson, D. D. Predicted Trends of Core−Shell Preferences for 132 Late Transition-Metal Binary-Alloy Nanoparticles. *J. Am. Chem. Soc.* **2009**, *131*, 14023−14029.
(68) Huang, R.; Wen, Y.-H.; Zhu, Z.-Z.; Sun, S.-G. Pt−Pd Bimetallic Catalysts: Structural and Thermal Stabilities of Core−Shell and Alloyed Nanoparticles. *J. Phys. Chem. C* **2012**, *116*, 8664−8671.
(69) Zhang, Z.-C.; Hui, J.-F.; Guo, Z.-G.; Yu, Q.-Y.; Xu, B.; Zhang, X.; Liu, Z.-C.; Xu, C.-M.; Gao, J.-S.; Wang, X. Solvothermal Synthesis of Pt-Pd Alloys with Selective Shapes and their Enhanced Electrocatalytic Activities. *Nanoscale* **2012**, *4*, 2633−2639.

DOI: 10.1021/acsami.6b11651
ACS Appl. Mater. Interfaces 2017, 9, 8030−8040